

Discovering the influence of lithium loss on Garnet $\text{Li}_7\text{La}_3\text{Zr}_2\text{O}_{12}$ Electrolyte Phase Stability

Andrea Paoletta^a, Wen Zhu^a, Giovanni Bertoni^{b,c}, Sylvio Savoie^a, Zimin Feng^a, Hendrix Demers^a, Vincent Gariépy^a, Gabriel Girard^a, Etienne Rivard^a, Nicolas Delaporte^a, Abdelbast Guerfi^a, Henning Lorrmann^d, Chandramohan George^e and Karim Zaghbi^{a,*}

^a Hydro-Québec, Center of Excellence in Transportation Electrification and Energy Storage, Varennes, Québec J0L 1N0, Canada

^b IMEM – CNR, Istituto dei Materiali per l'Elettronica e il Magnetismo, Parco Area delle Scienze 37/A, I-43124 Parma, Italy

^c CNR – Istituto Nanoscienze, Via Campi 213/A, I-41125 Modena, Italy

^d Fraunhofer-Institut für Silicatforschung ISC, Neunerplatz 2, 97082 Würzburg, Germany

^e Dyson School of Design Engineering, Imperial College London, SW7 2AZ, London, UK

Corresponding author: Zaghbi.karim@ireq.ca

SUPPORTING INFORMATION

METHODS SECTION

S₁ Synthesis

Undoped cubic LLZO synthesis

In a general undoped LLZO cubic synthesis 6,77 g of Li_2CO_3 , 11,64 g of La_2O_3 and 5,87 g of ZrO_2 are mixed in planetary mill with ZrO_2 balls under air atmosphere and then annealed in tubular furnace on graphite boat. The flow was kept at 2 L/min from room temperature to 700 °C and then it was stopped when the synthesis temperature was increased up to 950 °C and kept for 2 hours. 1 g of powder was annealed in static conditions and cooled down. On the contrary when 4 g of precursors are used tetragonal LLZO phase is obtained. It's important to underline that the graphite boat must not be porous. After each synthesis graphite become more and more porous and only tetragonal LLZO may be obtained instead of cubic LLZO.

Undoped tetragonal LLZO synthesis

In a general undoped LLZO tetragonal synthesis 6,77 g of Li_2CO_3 , 11,64 g of La_2O_3 and 5,87 g of ZrO_2 are mixed in planetary mill with ZrO_2 balls under air atmosphere and then annealed in tubular furnace on graphite (or zirconia or alumina) boat. The flow was kept at 2 L/min from room temperature to 700 °C and then the synthesis temperature was increased up to 950 °C and kept for 2 hours keeping N_2 gas flowing. Finally, the powder was cooled down.

Ga-doped cubic LLZO synthesis

In a general doped LLZO cubic synthesis 5,92 g of Li_2CO_3 , 11,39 g of La_2O_3 , 5,77 g of ZrO_2 and 0,56 g of Ga_2O_3 are mixed in planetary mill with ZrO_2 balls under air atmosphere and then annealed in tubular furnace on graphite (or zirconia or alumina) boat. The temperature was increased from room temperature to 700 °C and then the synthesis temperature was increased up to 950 °C and kept for 2 hours keeping N_2 gas flowing. Finally, the powder was cooled down.

In situ X-rays diffraction measurements

High temperature *in situ* X-ray (HTXRD) measurement was performed on a SmartLab diffractometer (Rigaku) with $\text{Co-K}\alpha$ radiation. The spectra were collected

every ~5 minutes with scan-step size 0.04°. The precursor powder was packed on a graphite sample holder and heated/cooled at a ramp rate of 30-40 °C/min and holding at 850 – 950 °C for desired time periods in nitrogen atmosphere with constant flow or cut off flow at certain temperatures.

S2. Ionic conductivity measurements

Densification process of LLZO pellets (undoped cubic, undoped tetragonal, cubic Ga doped) were all performed by annealing 1 mm thick pellet (13 mm diameter) at 1100 °C in air muffle furnace for 16 hours in alumina crucible surrounded by 1 gram of mother sacrificial powder. The final pellets were polished in glove box and a silver paste was deposited in both sides. The pellets were tested between two stainless steel spacers in coin-cells. Electrochemical impedance spectroscopy measurements were performed at 20, 40, 60 and 80 °C with an AC amplitude of 5 mV and a frequency range of 250 kHz to 10 mHz at 0.0 V versus open circuit voltage (OCV). The temperature dependence of the total ionic conductivity (Arrhenius plot) for each LLZO pellet can be expressed by the following Arrhenius equation, *eq.1*:

$$\sigma = (A/T)\exp(-E_a/k_B T) \quad \text{eq.1,}$$

where σ is the ionic conductivity, T the absolute temperature, A the pre exponential constant, k_B the Boltzmann constant and E_a is the activation energy for the ionic conductivity. E_a was determined from the slope of the $\log(\sigma T)$ versus $1/T$ plot.

S3 Morphology and elemental composition analysis

LLZO surfaces were analyzed using scanning electron microscope (SEM) Lyra 3 by TESCAN and elemental composition obtained using windowless energy dispersive spectrometer (EDXS) Extreme by Oxford instruments. Samples were cooled at -45 °C using a Deben peltier coolstage stage to prevent damage and heating of the LLZO during the observation. The micrograph and X-ray map were acquired at an accelerating voltage of 5 kV, a probe current of 500 pA, and a working distance of 10 mm.

S4 Transmission electron microscopy and chemical mapping

High resolution transmission electron microscopy images (HRTEM) and bright-field images in scanning mode (BF-STEM) were acquired on a JEOL JEM-2200FS

transmission electron microscope operated at 80 kV or 200 kV (point resolution 0.19 nm at 200 kV). Chemical mapping was performed using an energy dispersive X-ray spectrometer in scanning mode (STEM-EDXS) by measuring Ga-K and La-L X-ray lines. For the Li content, we used electron energy loss spectroscopy (STEM-EELS) from Li-K (~55 eV) and La-N (~115 eV) lines. The LLZO powder samples were grinded in toluene solution and deposited on holey-carbon support grids. The parameters of STEM-EELS acquisition were convergence semi-angle $\alpha = 11$ mrad and collection semi-angle $\beta = 8$ mrad). Conventional quantification techniques were applied as implemented in Gatan Digital Micrograph™ (Gatan, Inc.), consisting in pre-edge background extrapolation and subtraction using a power-law function, and modelling the ionization edges with atomic Hartree-Slater models (Egerton, 2011). We limited the analysis to crystals with a thickness $t/\lambda < 1.5$ (λ the inelastic mean free path), to keep a reliable quantification from the ionization edges. At higher thickness, the multiple scattering of plasmons severely reduces the accuracy in the extraction of the edges. At the condition of measurements, $\lambda = 115$ nm as calculated according to Malis et al.¹ and Everton et al.² **Figure S12** illustrates the Li-K and La-N_{4,5} quantification procedure from the spectrum image, considering the profile of **Figure 4c** of the manuscript as example. Due to the presence of the other low-loss edges in the pre-edge region of Li-K, complicating the extrapolation, and the low accuracy expected by using Hartree-Slater models for N_{4,5} edges, we assume a relative error in the quantification of Li/La of 20%. We did not quantify the Zr-N_{2,3} edge due to its overlapping with the plasmon peak from double scattering and the absence of a reliable model for N_{2,3} edges.

S5. Li₂CO₃ decomposition

Like almost all syntheses, side reactions can have an impact on the overall effect of the product. In this subsection, we discuss the premature decomposition of Li₂CO₃, which by producing Li₂O reduces the accessibility of part of the lithium. We believe that it is the relative reaction rate of Li₂CO₃ decomposition and its reaction with other solid precursors that controls the lithium loss. This relative rate is in turn controlled by the CO₂ concentration with the N₂ gas flow.

When the partial pressure of CO₂ approaches or reaches the equilibrium partial pressure of CO₂ for the reaction,

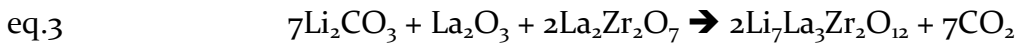


the decomposition of Li_2CO_3 significantly slows down or stops completely. For the readers' convenience, we adopt from the literature³⁻⁵ the equilibrium CO_2 pressures at atmospheric pressure as a function of temperature in Table S1, where the units are changed to SI. Since at these temperatures the gas is well described by the ideal gas model, the partial pressures of CO_2 can be safely represented by the CO_2 concentration, as presented in the 3rd row of Table S1.

T (K)	883	996	1083	1161	1238
P (Pa)	133	533	2000	4266	8398
Ratio (%)	0.13	0.53	1.97	4.21	8.29

Table S1: Equilibrium CO_2 pressure of Li_2CO_3 decomposition. Adopted from (cite report 3). The melting point of Li_2CO_3 at ambient pressure is 996 K.

During the synthesis of LLZO, this side reaction of Li_2CO_3 decomposition creates Li_2O pellets, which are quite stable at our synthesis temperature, and it is difficult to incorporate them into the desired final product LLZO. The best scenario for us is that Li_2CO_3 melts and mixes well with LZO without CO_2 emission and then emits CO_2 to finish the final step (eq. 3).



However, it is evidently impossible to completely prevent the premature decomposition of Li_2CO_3 . On the other hand, the reaction between Li_2CO_3 and $\text{La}_2\text{Zr}_2\text{O}_7$ and La_2O_3 takes place simultaneously, but because of the incorporation of Li_2O into LZO; i.e., the formation of LLZO is exothermic, the equilibrium partial pressure of reaction (3) will be higher than that of reaction (2). While the presence of CO_2 tends to suppress both reactions, its suppression of reaction (3) is more stringent. It is commonly accepted that reactions between solids are slower than reactions involving only liquid and gas. In our case, above 750 °C, we have liquid Li_2CO_3 , gaseous CO_2 , solid LZO and, from the decomposition of Li_2CO_3 , solid Li_2O . Therefore, without environmental CO_2 , Li_2CO_3 will decompose the fastest,

producing Li_2O , whose reaction with LZO to form LLZO is the slowest. Suppressing Li_2CO_3 decomposition reduces premature CO_2 emission but leaves solid LZO to react with liquid Li_2CO_3 faster and, due to the closer contact of solid-liquid than solid-solid interfaces, more reliably than with solid Li_2O .

To this end, we enclosed the reactants in a chamber with the N_2 gas flow shut off to create a CO_2 -rich environment, where CO_2 comes from inevitable Li_2CO_3 decomposition.

The effect of this decomposition suppression is quite phenomenal, as impurities due to the loss of lithium are drastically reduced. From a theoretical point of view, we calculated gas diffusion by solving the CO_2 concentration inside the chamber during the hour of the synthesis. We refer the readers to the Methods section for the details of this calculation. Briefly, we wished to see how CO_2 emission (from the Li_2CO_3 decomposition) affects the CO_2 partial pressure around the sample, which in turn affects the rate of Li_2CO_3 decomposition. If, in the end, we find a CO_2 concentration close to or higher than that at equilibrium, we can conclude that the decomposition of Li_2CO_3 will be suppressed; if it is far less than that, the decomposition shall not be affected significantly.

Without further knowledge, we assumed a constant temperature of 750°C , i.e., the temperature when Li_2CO_3 starts to decompose, and a 2-dimensional model. The rate of CO_2 emission was also assumed to be uniform over the hour, which translates to a constant CO_2 injection rate of 0.05 g/hour through the surface of the sample. The dimension of the chamber was $\text{Ø}7\text{ mm} \times 1476\text{ mm}$, where the gas flow can be controlled. The sample is placed near the middle of the chamber. The CO_2 injection rate is proportionally adjusted to provide a realistic concentration. Since we are most interested in the concentration profile in the longitudinal section of the chamber, we believe this simplified 2-dimensional model suffices.

S6-Numerical Methods

The numerical simulation of CO_2 emissions in a still nitrogen atmosphere was carried-out using Ansys Fluent. A 2D geometry was used to model the tubular oven. One end of the oven is modeled with a “velocity inlet” where velocity is set to 0 (see label C of **Figure 5**). The other end where a check valve is present is modeled using an “outlet vent” boundary conditions that basically acts as a restriction (see label A of **Figure 5**). All other surfaces are walls where net diffusive and heat transfer fluxes do not occur. CO_2 is introduced at a rate of 0.1 g/h in the simulation domain by

means of source terms within the species model (see area labeled B in **Figure 5**). **Figure 5a** shows the CO₂ concentration gradient after 1 hour. The CO₂ concentration at the surface of the sample reaches 12%.

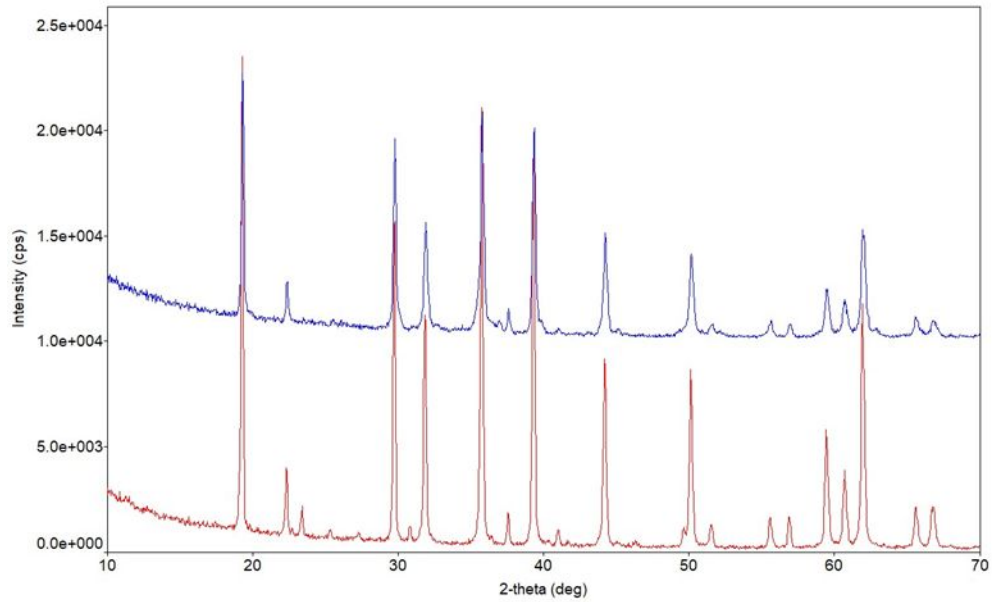


Figure S1 XRD spectra of Ga-LLZO (red) and un-doped LLZO (blue) cooled to RT.

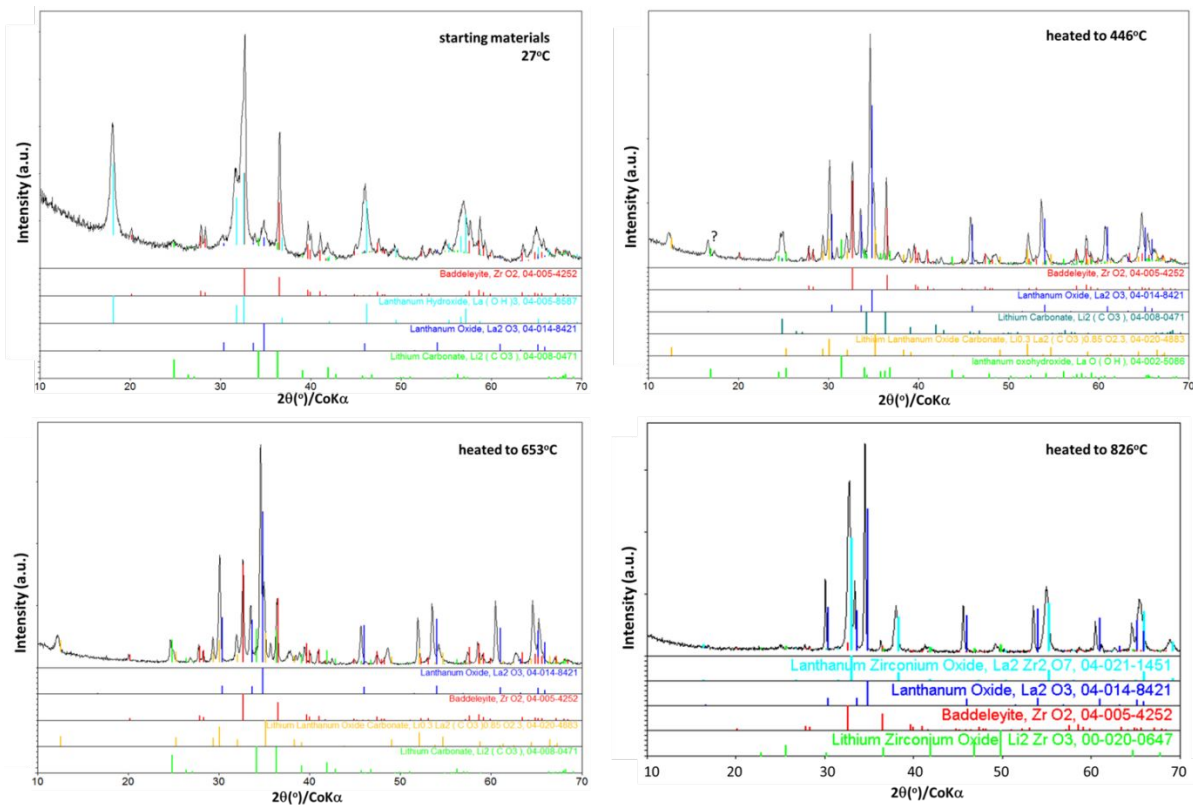


Figure S2. in situ XRD patterns of undoped LLZO from 26 °C to 826° C with N_2 constant gas flow.

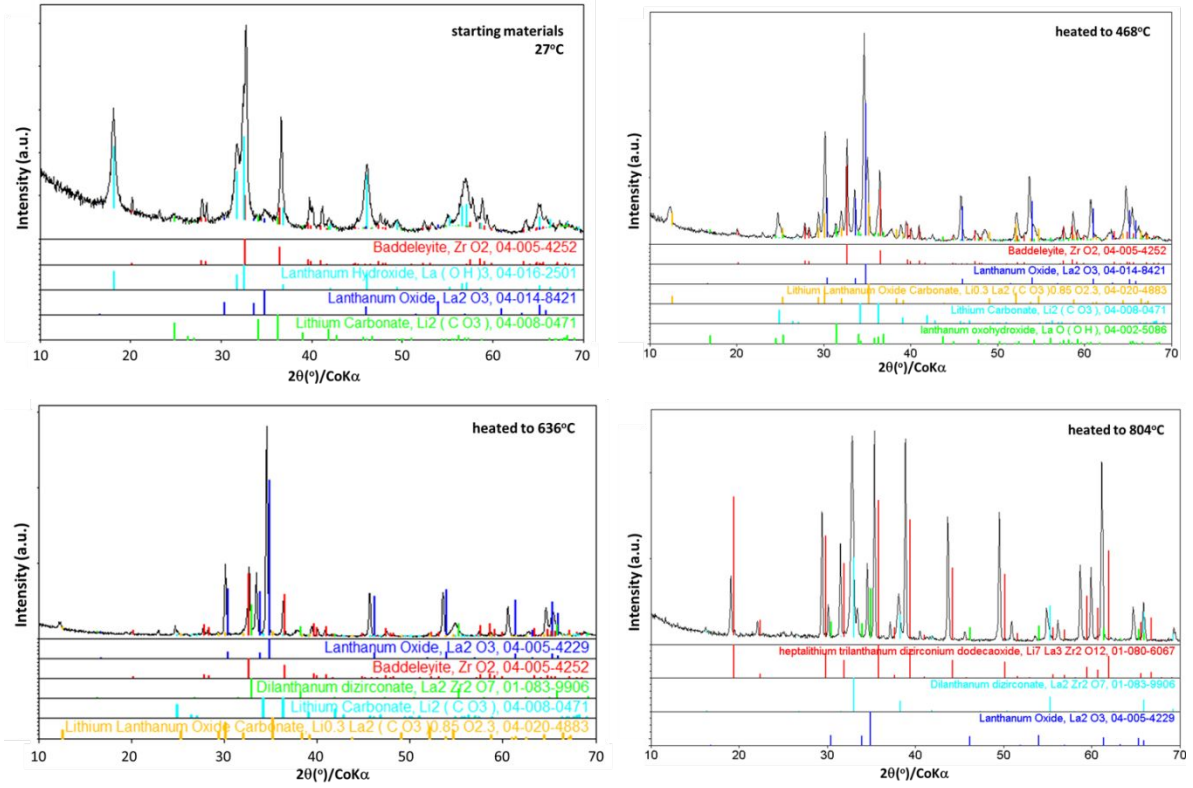


Figure S3, in situ XRD patterns of undoped LLZO from 26 °C to 804 °C with stop gas flow.

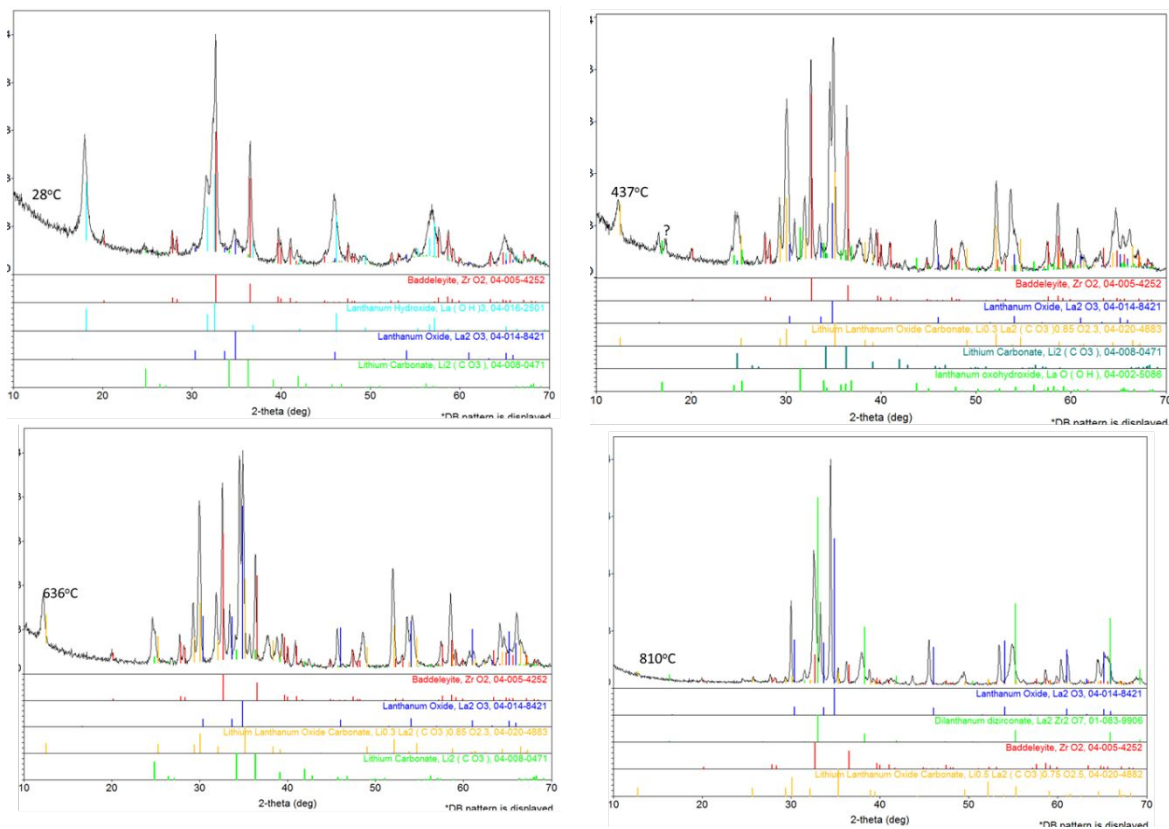


Figure S4. In-situ XRD patterns of undoped LLZO from 26 °C to 804° C with stop gas flow.

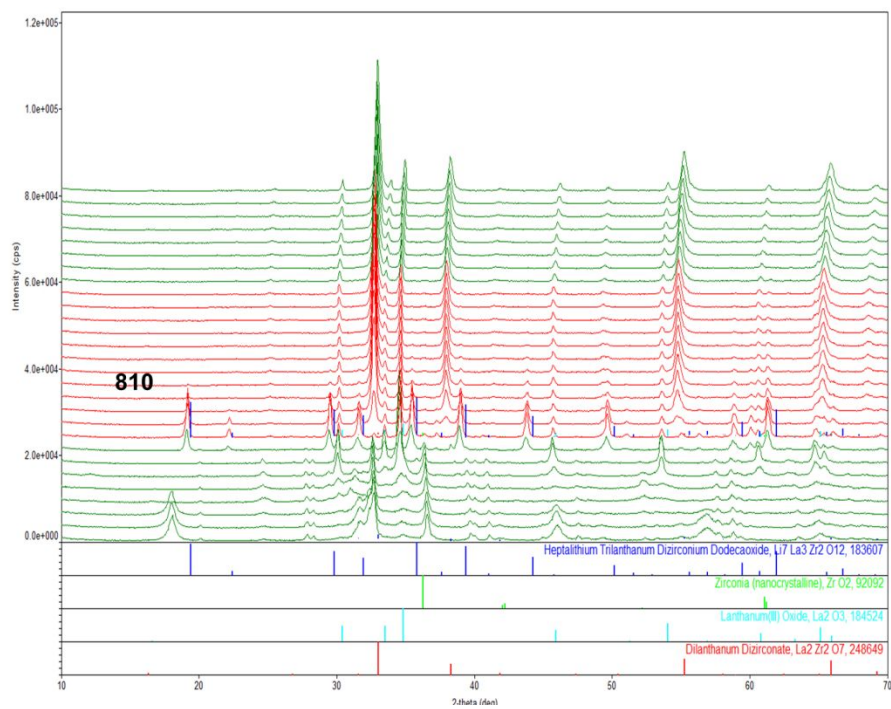


Figure S5. In-situ XRD patterns of undoped LLZO under vacuum.

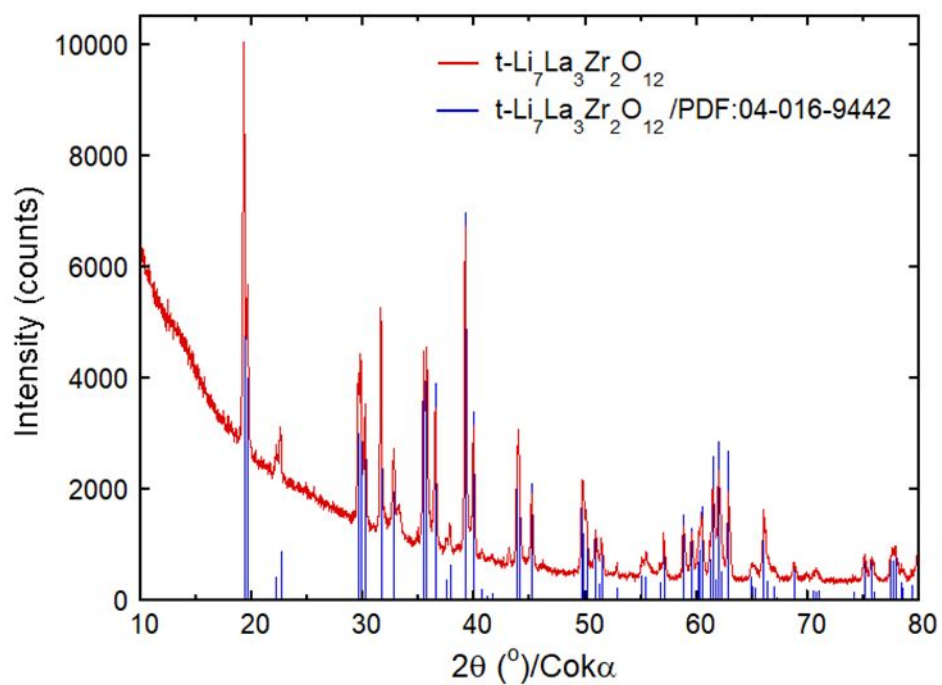


Figure S6: tetragonal LLZO obtained annealing 4 gr instead of 1 gram in tubular furnace with gas flow.

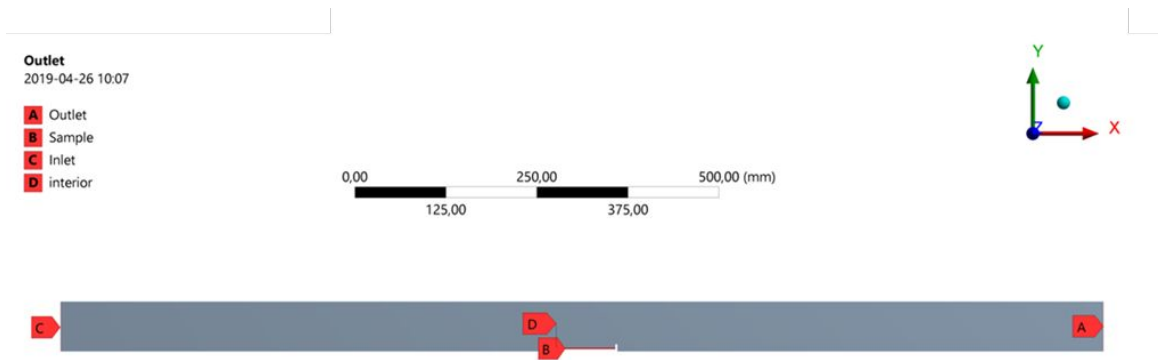


Figure S7. *Schematic representation of tubular furnace.*

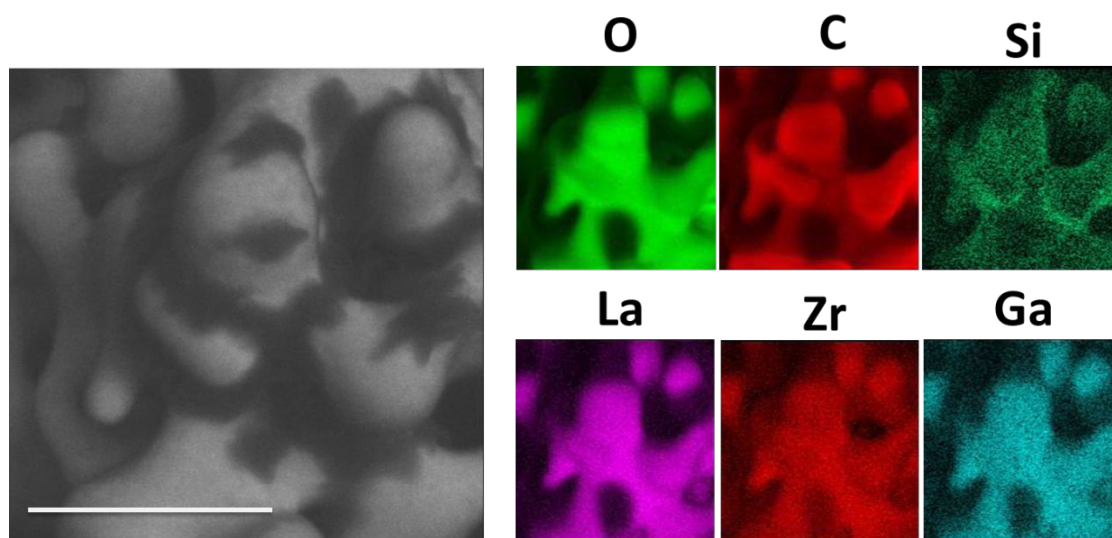


Figure S8. SEM backscattered electron image of Ga:LLZO after synthesis and EDS mapping.

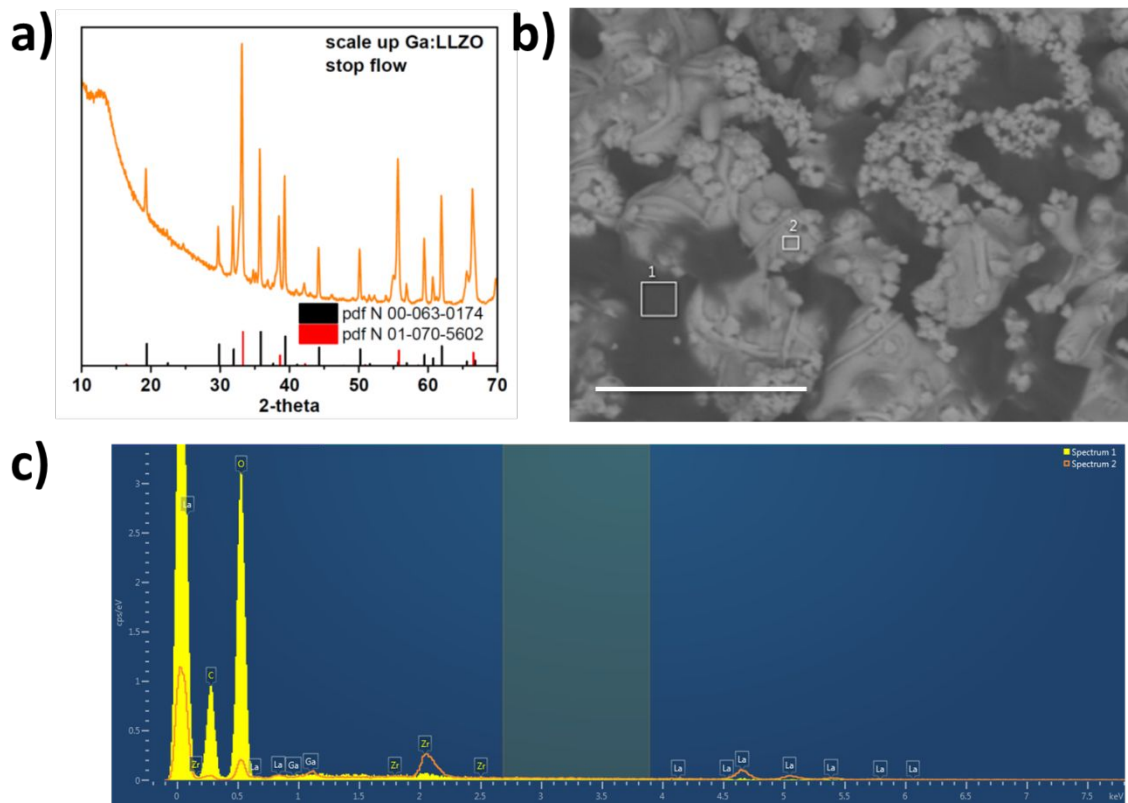


Figure S9. a) XRD pattern, b) SEM image and c) EDS spectrum of scale up Ga:LLZO synthesized with no gas flow.

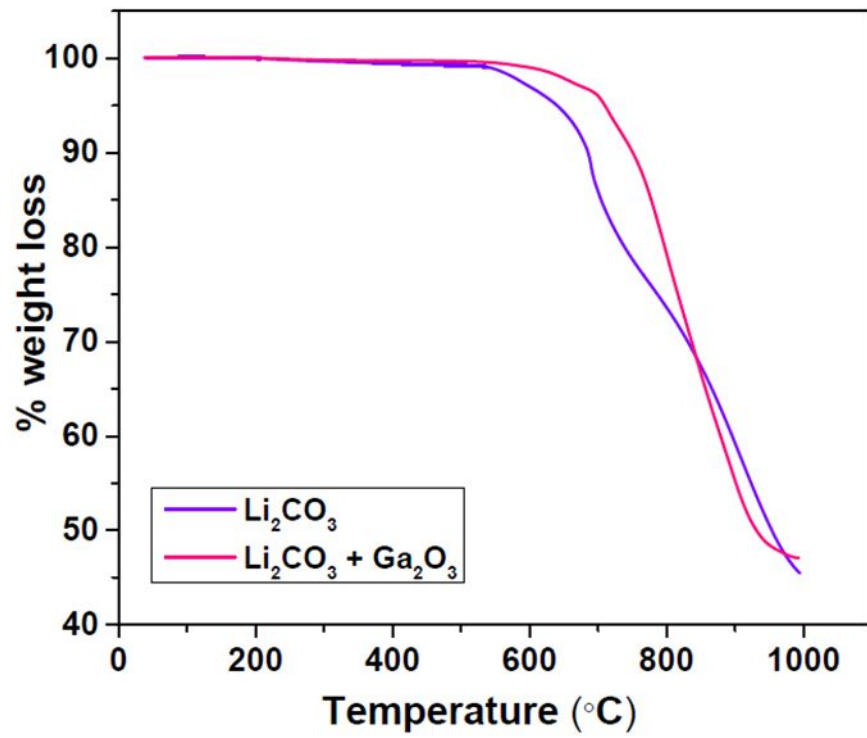


Figure S10. Thermogravimetric analysis of Li_2CO_3 and $\text{Li}_2\text{CO}_3 + \text{Ga}_2\text{O}_3$.

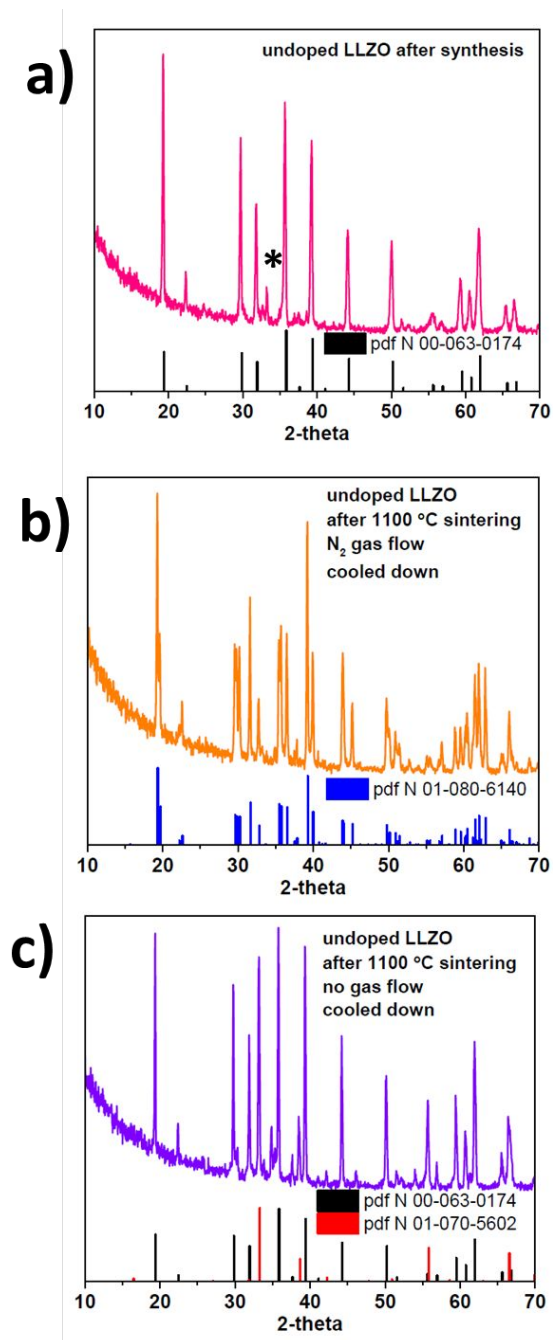


Figure S11. XRD pattern of a) undoped LLZO after synthesis, b) undoped LLZO after sintering under N₂ flow and c) undoped LLZO after sintering with no gas flow.

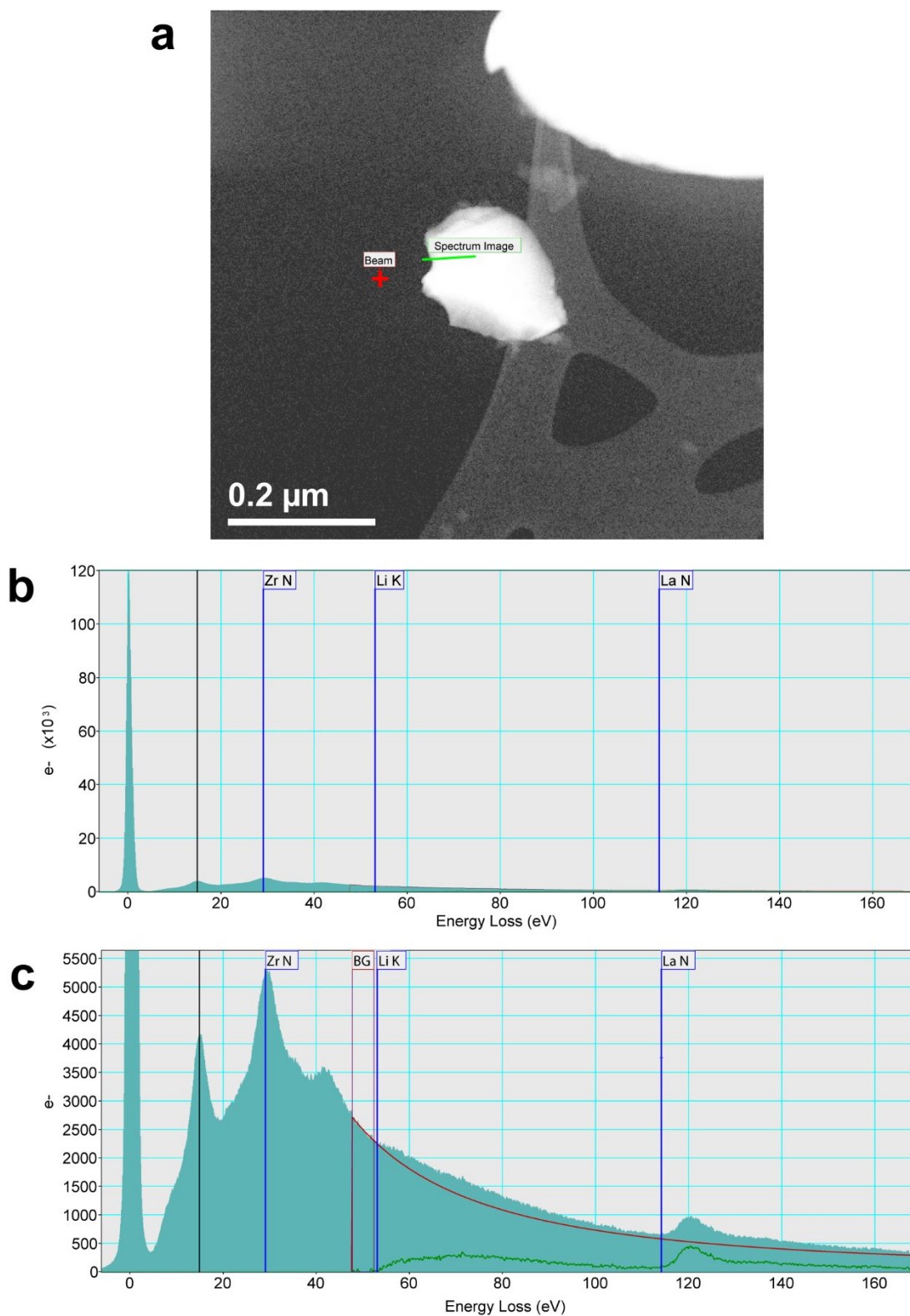


Figure S12. *a*) Annular dark field (ADF-STEM) survey image for the particle from Figure 4c of the manuscript. The spectrum image for the EELS profile is in green. The red cross indicates the beam parking position in vacuum before the spectrum image acquisition. *b*) The extracted

spectrum from the inner point of the spectrum image. From the intensity of the elastic peak with respect to the total area of the spectrum (log-ratio method) we estimated a thickness $t/\lambda = 0.99$, which corresponds to $t \sim 113$ nm. c) Enlarged view of the spectrum from a). A plasmon at 15 eV is indicated, together with the Zr-N_{2,3} edge, The Li-K edge, and La-N_{4,5} edge. For better reading, the La-N_{4,5} edge is shifted by +15 eV to accounts for the delayed offset as expected for high-shell electrons. The Li-K edge onset is broadened by multiple scattering at the present thickness. We opted for extrapolating the conventional power-law background (BG) in the pre-edge region for Li-K while keeping a low but positive residual intensity in the pre-edge region of La-N_{4,5} (see the full red line in the spectrum).

References

- 1 Malis, T., Cheng, S. C., & Egerton, R. F. (1988) EELS log-ratio technique for specimen-thickness measurement in the TEM. *J. Elec. Microsc. Tech.*, 8(2), 193-200.
<https://doi.org/10.1002/jemt.1060080206>
- 2 Egerton, R.F., *Electron Energy-Loss Spectroscopy in the Electron Microscope*, Third Edition, Springer: Boston, MA (2011).
- 3 Kroll, W. J., & Schlechten, A. W. (1947). Laboratory Preparation of Lithium Metal by Vacuum Metallurgy. *American Institute of Mining and Metallurgical Engineers*, (June).
- 4 Ktalkherman, M. G., Emelkin, V. A., & Pozdnyakov, B. A. (2009). Production of Lithium Oxide by Decomposition Lithium Carbonate in the Flow of a Heat Carrier. *Theoretical Foundations of Chemical Engineering*, 43(1), 93-98.
<https://doi.org/10.1134/S0040579509010114>
- 5 Pozdnyakov, B. A., & Zamyatin, A. P. (2008). High-Temperature Decomposition of Lithium Carbonate at Atmospheric Pressure. *High Temperature*, 46(3), 414-421.
<https://doi.org/10.1134/S0018151X0803019X>